Approaching the ultrastrong-coupling regime between an Andreev level and a microwave resonator

Citation for the original published paper (version of record):

Shvetsov, O., Khola, A., Buccheri, V. et al (2025). Approaching the ultrastrong-coupling regime between an Andreev level and a microwave resonator. Physical Review Applied, 24(4). http://dx.doi.org/10.1103/f81h-xjcv

Approaching the ultrastrong-coupling regime between an Andreev level and a microwave resonator

O. O. Shvetsov,* A. Khola, V. Buccheri, I. P. C. Cools, N. Trnjanin, and A. Geresdi
Department of Microtechnology and Nanoscience, Chalmers University of Technology, SE-41296 Gothenburg, Sweden

T. Kanne and J. Nygård
Niels Bohr Institute, Center for Quantum Devices, University of Copenhagen, Universitetsparken 5, DK-2100 Copenhagen O, Denmark

(Received 17 February 2025; revised 5 June 2025; accepted 12 September 2025; published 6 October 2025)

Josephson junctions formed in semiconductor nanowires host Andreev bound states and serve as a physical platform to realize Andreev qubits tuned by electrostatic gating. With the Andreev bound state being confined to the nanoscale weak link, it couples to a circuit-QED architecture via the state-dependent supercurrent flowing through the weak link. Thus, increasing this coupling strength is a crucial challenge for this architecture. Here, we demonstrate the fabrication and microwave characterization of a weak link which is defined in an InAs-Al (core-half shell) nanowire and embedded in a superconducting loop with a lumped-element resonator patterned from a thin NbTiN film with high kinetic inductance. We investigate several devices with various weak-link lengths and performed spectroscopy that revealed pair transitions and single-quasiparticle transitions arising from spin-orbit-split Andreev bound states. Our approach offers a compact geometry and a large resonator impedance above 12 kΩ at a resonator frequency of 8 GHz, which facilitates large coupling in the system. For the pair transitions, the experimentally observed energy level splitting demonstrates the coupling to an Andreev level of 490 MHz. We apply a perturbative model that shows good agreement with the experimental data and extract the maximum coupling of 968 MHz. Moreover, we show that the coupling is even stronger to an Andreev level with a higher transmission. In addition, spectroscopy of single-quasiparticle transitions reveals spin-orbit-split Andreev bound states with the extracted spin-photon coupling of 77 MHz.

DOI: 10.1103/f81h-xjcv

I. INTRODUCTION

Circuit-QED (CQED) describes the interaction of photons stored in a superconducting resonator and a two-level system (qubit) [1]. The latter is often based on a single electron spin [2] or collective excitations in various superconducting circuits [3,4]. For quantum information processing, the favorable regime is when the qubit is strongly coupled to the resonator, that is, when they exchange a photon many times before the coherence is lost [4].

A distinct ultrastrong-coupling regime is established when the coupling strength becomes a significant fraction of the bare resonator and qubit frequencies [5–7]. In this case, the common rotating-wave approximation is no longer valid and more comprehensive models are applied [8]. From a practical point of view, the ultrastrong-coupling regime has been proposed to be used, for example, for ultrafast quantum computation [9].

Andreev bound states (ABSs) are discrete fermionic excitations spatially confined in a weak link between two superconductors [10,11]. Atomiclike transitions between these states can be utilized for the realization of two types of qubits, namely Andreev pair qubit [12–16] and Andreev spin qubit [17–23], which can be experimentally investigated by the means of CQED techniques [24–26]. Semiconductor nanowires serve as the preferred platform for such experiments, due to high material quality, gate tunability, and intrinsically strong spin-orbit coupling [27], which opens the way to exploit not only the charge, but also the spin degree of freedom in qubit applications. The possibility of coupling a single quasiparticle spin to macroscopic supercurrents makes Andreev qubits a promising alternative to traditional spin and superconducting qubit platforms [18,28,29].

*Contact author: shvetsov@chalmers.se

In conventional superconducting circuits, qubits are formed from quantized energy levels of collective electromagnetic excitations. In contrast, ABSs are localized within the weak link and carry a supercurrent up to the range of 10 nA for the typical geometry of InAs nanowires [30]. This makes it more challenging to reach strong coupling to a microwave resonator. In practice, the coupling is typically realized by embedding a phase-biased weak link in a superconducting loop with a part of the resonator, also referred to as a shared inductance. In this case, the coupling rate g_c is proportional to the zero-point flux (phase) fluctuations across the shared inductance [24], which is in turn proportional to the square root of the resonator impedance Z_r, resulting in $g_c \propto \sqrt{Z_r}$ [31,32]. Thus, an increase in the resonator impedance naturally leads to a stronger coupling, enabling better resolution spectroscopy and making higher-energy states accessible.

In this paper, we investigate several devices that integrate a lumped-element resonator made of a thin NbTiN film and a weak link tailored in an InAs-Al (core-half shell) nanowire. Because of the high kinetic inductance of the NbTiN film, the differential impedance of the resonator reaches values above 12 kΩ. We perform single- and two-tone spectroscopy that revealed pair and single-quasiparticle transitions. The system exhibits large energy splitting at the avoided crossings, which indicates the coupling to an Andreev level of 490 MHz, and the model predicts that the coupling reaches up to 968 MHz. Moreover, we show that coupling to an Andreev level with a higher transmission can reach the value of 1.95 GHz, more than 20% of the bare resonator frequency. Our findings suggest that the system is approaching the ultrastrong-coupling regime. In addition, we demonstrate that the presented geometry can be used to resolve spin-orbit-split ABSs, and we extract the coupling to an Andreev spin of 77 MHz.

II. DEVICE AND SETUP

The devices used in this work consist of a weak link which is defined in an InAs nanowire [27] and embedded in a superconducting loop with a high-impedance lumped-element resonator. We report on fabrication and measurement of three devices, where the resonator geometry and the weak-link length vary. Their parameters are listed in Table I. A representative device (a replica of device 2) is demonstrated in Fig. 1(a) and is described below.

The resonator is patterned on a sapphire substrate with a thin (around 6 nm) sputtered film of a highly disordered NbTiN superconductor. Figure 1(b) represents an electron micrograph of the resonator structure. It consists of a differential pair of 130-nm-wide and 38.3-μm-long symmetric arms, divided by the grounding strip in the middle. Each arm is terminated with a triangular-shaped capacitor plate that is coupled to a 50-Ω feedline. When these feedlines are driven differentially, the microwave signal oscillates in the arms with opposite phase, which is also referred to as the odd mode. In the even mode, on the contrary, microwaves in the two arms oscillate in-phase. Because of the high kinetic inductance of the thin film, $L_{k,\square} \approx 400$ pH, this compact structure with a footprint of 50×50 μm^2 realizes a total inductance $L_r \approx 118$ nH and resonates in the odd mode at the frequency $f_r = 8.619$ GHz as a lumped-element resonator. The differential impedance of the resonator reaches $Z_{r,\mathrm{diff}} = 2\sqrt{L_r/C_r} \approx 12.76$ kΩ.

TABLE I. Parameters of the devices, including length, width, and differential impedance of the resonators, thin-film kinetic inductance, bare resonator frequency, zero-point flux fluctuations across the shared inductance, and the weak-link length.

Device	Length[a] (μm)	Width (nm)	$Z_{r,\mathrm{diff}}$ (kΩ)	$L_{k,\square}$[b] (pH)	f_r (GHz)	Φ_{zpf}[c] (Φ_0)	l_{wl} (nm)
1	48.3	130	12.28	320	8.2230	0.016	250
2	38.3	130	12.76	400	8.6190	0.021	320
3	53.3	130	13.27	345	7.4685	0.015	450

[a]Length of one arm of the differential pair.
[b]May vary due to sample aging and slightly different fabrication parameters.
[c]Deduced from the resonator geometry and inductance.

The weak link was defined in a 150-nm-thick MBE-grown InAs nanowire with an *in-situ*-grown epitaxial Al shell covering three of its facets [27]. A 250- to 450-nm-long part of the 27-nm-thick Al shell was removed by wet etching [33]; an example is shown in Fig. 1(c). A small part of the resonator with the shared inductance $2l \approx 12.3$ nH is coupled to the nanowire by incorporating it in a common superconducting loop with Al contacts. The weak link couples to the odd mode of the resonator, because in the even mode the currents through the shared inductance cancel out. In this geometry, the coupling between the ABSs and the resonator is proportional to the zero-point flux fluctuations across the shared inductance $\Phi_{\mathrm{zpf}} = (l/L_r)\sqrt{\hbar Z_{r,\mathrm{diff}}/2} \approx 0.021\Phi_0$, where $\Phi_0 = h/2e$ is the superconducting flux quantum. The shared inductance was intentionally designed to be large, but comparable to the weak-link Josephson inductance, which ensures that the phase across the junction φ is a nonhysteretic function of the applied flux Φ. Moreover, our analysis shows that $\varphi \approx 2\pi\Phi/\Phi_0$ is a reasonable approximation (see Appendix D).

A dc electrostatic side gate is defined at a distance of 150 nm away from the junction to tune the electrochemical potential in the nanowire. The differential drive and the overall symmetric chip layout ensure that, along the mirror line, the ac electric field is essentially zero. To reference the nanowire to the dc ground potential, the nanowire loop is connected to the ground by a metal strip located along

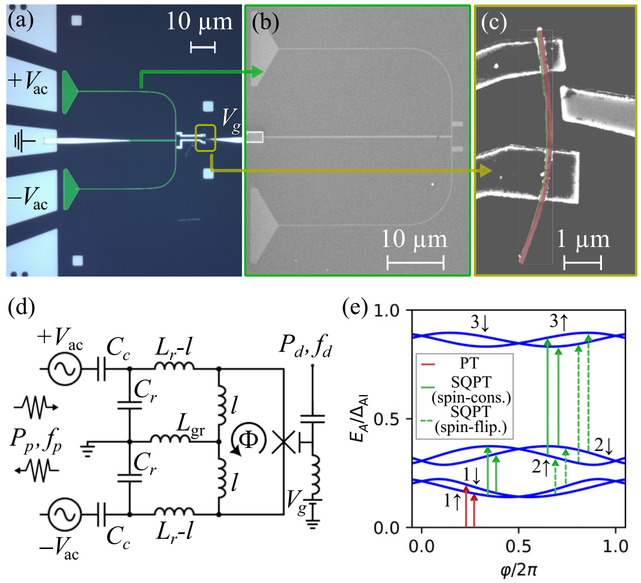

FIG. 1. (a) An optical micrograph of a representative device. The resonator is denoted by a green (false color) U-shaped structure patterned from a thin NbTiN film with high kinetic inductance. The resonator is capacitively coupled to a pair of feedlines. A weak link in an InAs-Al nanowire is defined close to the mirror line of the device and coupled to the resonator by aluminum contacts. (b) Electron micrograph of a test resonator structure fabricated simultaneously with the studied device on the same chip. (c) Electron micrograph of the nanowire (false color) with a weak link, Al leads, and a side gate. (d) Circuit diagram showing an equivalent lumped-element scheme of the device. It consists of a differential pair of resonators with the inductances L_r and capacitances C_r, coupled to the feedlines by the capacitors C_c. The nanowire weak link is embedded in a flux-biased superconducting loop with a small fraction of the resonator with the shared inductance $2l$. To ground the loop, the resonator's middle part is connected with the ground plane. The resonator is probed in reflection with the probe signal of power P_p and frequency f_p. The side gate is used to tune the nanowire's electrochemical potential and to excite the system with a drive signal of power P_d and frequency f_d. (e) Typical excitation spectrum of a long weak link with spin-orbit interaction. Three ABSs are present in the spectrum, each of them being split into a doublet of states with the opposite pseudospin, denoted by ↑ and ↓. Microwave photons can induce pair transitions (PT, red arrows) and single-quasiparticle transitions (SQPT, green arrows), where, for the latter, spin-conserving (solid) and spin-flipping (dashed) processes can be distinguished. The energy scale is normalized to the superconducting gap in Al.

this line, which does not disturb the resonator's odd mode. In such a design, having the nanowire weak link defined at the zero ac voltage line is preferable to mitigate microwave losses through the side gate. A superconducting coil was used to flux-bias the weak link. The circuit diagram of the device is presented in Fig. 1(d).

The odd mode of the resonator is probed in reflection with the signal of power P_p and frequency f_p. A separate microwave tone passes through a bias tee to the side gate to excite the system with a drive signal of power P_d and frequency f_d.

After fabrication, the device chip is wire-bonded to a printed circuit board and embedded in a copper box attached to the mixing chamber of a dilution refrigerator with a base temperature of 10 mK. To screen spurious magnetic fields in the laboratory, an additional aluminum shield wrapped with magnetic shielding foil was installed.

The system represents a typical CQED setup, where microwave photons drive transitions between ABSs, and the state of the system can be detected by the resonator dispersive shift. One of the defining parameters of the ABS spectrum in a weak link is the ratio between the weak-link length $l_{\rm wl}$ and the superconducting coherence length ξ, which is typically several hundred nanometers in InAs nanowires proximized by aluminum. To describe the excitation spectrum in a finite-length weak link with $l_{\rm wl}/\xi \sim 1$, we refer to the model employed in Refs. [19,34]. The minimal model that includes spin-orbit splitting requires two transverse subbands. In this case the energy dispersion $\epsilon = E_A/\Delta_{\rm Al}$ of the ABSs is a solution to the transcendental equation:

$$\begin{aligned}\tau \cos[(\Lambda_1 - \Lambda_2)\epsilon \mp \varphi] + (1-\tau)\cos[(\Lambda_1 + \Lambda_2)\epsilon x_0] \\ = \cos[2\arccos\epsilon - (\Lambda_1 + \Lambda_2)\epsilon]. \qquad (1)\end{aligned}$$

Here τ is the channel transmission, $\Delta_{\rm Al}$ is the Al superconducting gap, $x_0 \in [-1, 1]$ indicates the position of a barrier in the weak link (normalized to $l_{\rm wl}/2$), and $\Lambda_j = l_{\rm wl}\Delta_{\rm Al}/\hbar v_{Fj}$, where v_{Fj} is the Fermi velocity of the subband $j = 1, 2$ in the nanowire.

In a finite-length weak link, multiple ABSs can squeeze into the spectrum; e.g., three levels are shown in a characteristic spectrum illustrated in Fig. 1(e). Spin-orbit interaction lifts the spin degeneracy, splitting each of the states into a doublet with the opposite pseudospin, denoted by ↑ and ↓. The time-reversal symmetry preserves degeneracy only at $\varphi = 0$ and $\varphi = \pi$. We consider two types of transitions: a pair transition (PT, red arrows) takes place when two quasiparticles are excited from the ground state; a single-quasiparticle transition (SQPT, green arrows) occurs when a quasiparticle that is already present in the system is promoted to one of the upper levels. Among SQPTs, spin-conserving (solid) and spin-flipping (dashed) transitions can be distinguished, when the transition is between the levels with the same or opposite pseudospin, respectively.

III. RESULTS AND DISCUSSION

We first present the typical microwave gate response, obtained for device 2. The change in the absolute value of

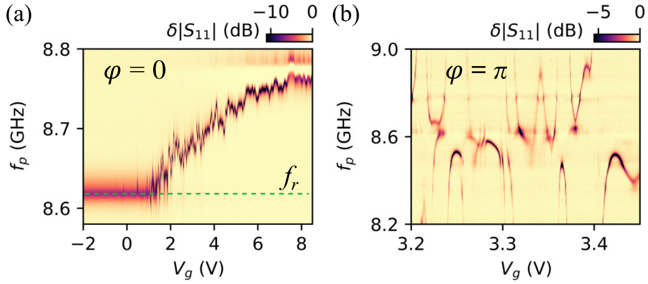

FIG. 2. Change in the absolute value of the resonator reflection $\delta|S_{11}|$ as a function of the probe frequency f_p and gate voltage V_g measured in device 2 at (a) $\varphi = 0$ and (b) $\varphi = \pi$. The line at $f_r = 8.619$ GHz in panel (a) denotes the bare resonator frequency, when the nanowire is fully pinched off. The gate-independent background was subtracted.

the resonator reflection $\delta|S_{11}|$ as a function of the probe frequency f_p and side-gate voltage V_g is presented in Fig. 2 (the gate-independent background is subtracted). In Fig. 2(a), the phase across the weak link φ is fixed at zero, while $\varphi = \pi$ in Fig. 2(b). The junction is fully pinched off below $V_g \approx 1$ V, where the resonance approaches the bare resonator frequency $f_r = 8.619$ GHz. The data obtained at $\varphi = \pi$ in Fig. 2(b) demonstrate multiple avoided crossings, signifying that the ABSs are strongly coupled to the resonator mode.

Further, we performed single- and two-tone spectroscopy to characterize the system. To mitigate charge noise and avoid electrostatic drifting, in these measurements we fix the gate voltage V_g at one of the points where the resonator gate response has a local extremum, such as one of those observed in Fig. 2(b). Single-tone spectra are taken by sweeping the probe frequency f_p of power P_p and measuring complex parameters S_{11} at various applied fluxes. The flux-independent background was subtracted in the data plotted. When the two-tone spectra were measured, we first performed a single-tone frequency sweep to define the resonance position at a certain phase (flux). Then, a continuous-wave probe tone was fixed at this frequency and S_{11} was measured as a function of the drive tone with frequency f_d and power P_d. To reference the signal measured in two-tone spectra, we subtracted a drive-frequency-independent background.

A. Spectroscopy of pair transitions

Figure 3 presents the spectroscopy data for device 2. Data were acquired at $V_g = 3.39$ V and at the nominal powers $P_p \approx -130$ dBm and $P_d \approx -100$ dBm. Figure 3(a) illustrates the two-tone spectrum, which reveals a PT arising from a highly transmissive ABS. It crosses the odd mode of the resonator, forming a pair of avoided crossings at $\varphi/2\pi = 0.4$ and $\varphi/2\pi = 0.6$, where

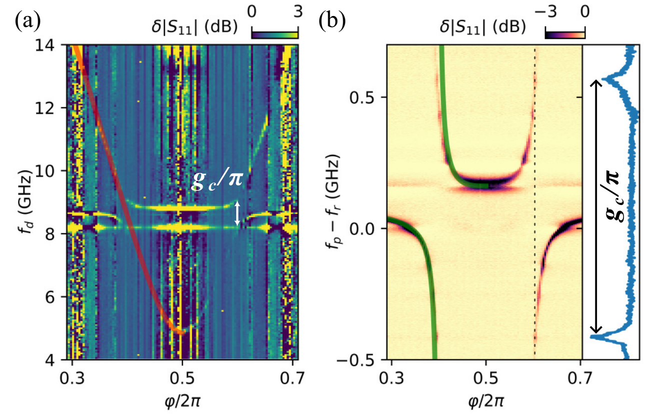

FIG. 3. (a) Two-tone spectrum measured in device 2 at $V_g = 3.39$ V. The fit of the PT frequency as a function of phase is shown by the red line. The spectrum reveals avoided crossings at $\varphi/2\pi = 0.4$ and $\varphi/2\pi = 0.6$ with the coupling at the crossings $g_c/2\pi \approx 490$ MHz, denoted by the white arrow. The flat line seen at around 8.1 GHz corresponds to the resonator's even mode, which is insensitive to the state of the weak link. (b) Corresponding single-tone spectrum. The probe frequency f_p is offset to the bare resonator frequency $f_r = 8.619$ GHz. The green line represents the fit of the resonator shift. The line cut on the right-hand side clearly confirms that $g_c/2\pi \approx 490$ MHz at the avoided crossing [along the gray dotted line in panel (b)].

the coupling can be directly extracted from the level splitting on resonance $g_c/2\pi \approx 490$ MHz.

In the vicinity of $\varphi = \pi$, the PT frequency can be fitted to the dispersion relation valid for a short weak link,

$$hf_{\mathrm{PT}} = 2E_A = 2\Delta'\sqrt{1 - \tau \sin^2(\varphi/2)}, \qquad (2)$$

respecting the fact that the effective gap value in a finite-length weak link is smaller than the gap in aluminum, $\Delta' < \Delta_{\mathrm{Al}}$ (see Appendix C for details). The least-squares method yields $\Delta'/h = 11.69 \pm 0.03$ GHz and $\tau = 0.9569 \pm 0.0005$. The resulting fit is represented as a red line in Fig. 3(a).

Figure 3(b) shows the corresponding single-tone spectrum. The coupling at the avoided crossing $g_c/2\pi \approx 490$ MHz can be directly extracted from the line cut along the gray dotted line (see the right-hand side of the plot). The green line denotes the fit that was obtained from the model described in Appendix C. The fit relies on a single ABS observed in the two-tone spectrum in Fig. 3(a). We confirmed that no higher-energy states are observed up to $f_d = 21$ GHz (see Appendix F). In the fit, the zero-point flux fluctuation across the shared inductance is the only fitting parameter. The least-squares fit to the experimental data yields $\Phi_{\mathrm{zpf}} = (0.0282 \pm 0.0002)\Phi_0$, which slightly overshoots the value obtained from the geometry analysis (see Table I). To validate the fit, we extract the magnitude of the coupling at the avoided crossing $g_c/2\pi = 495 \pm 4$ MHz,

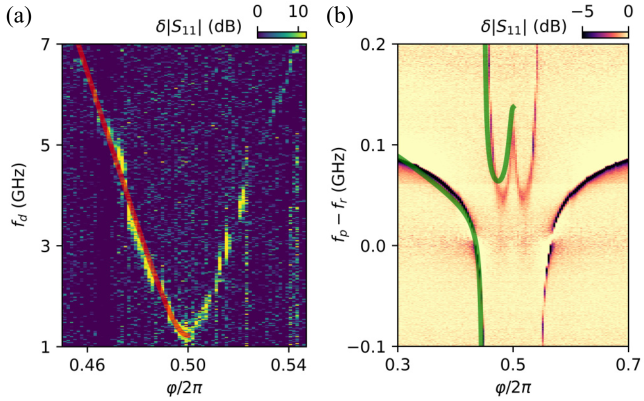

FIG. 4. (a) Two-tone spectrum measured in device 1 at $V_g = 14.5$ V. The PT frequency fit plotted as a function of phase is denoted by the red line. (b) Corresponding single-tone spectrum. The probe frequency f_p is offset to the bare resonator frequency $f_r = 8.223$ GHz. The green line denotes the fit of the resonator shift.

which is in good agreement with the observed energy splitting. The maximum coupling can be extracted at $\varphi = \pi$: $g_c/2\pi = 968 \pm 7$ MHz.

Figure 4 provides the spectroscopy data obtained for device 1 with the shortest 250-nm weak link at $P_p \approx -130$ dBm and $P_d \approx -100$ dBm, and at $V_g = 14.5$ V (this device required a higher gate voltage due to the longer distance to the gate). Here, we were following a similar fitting routine. The two-tone spectrum in Fig. 4(a) is fitted by Eq. (2) describing a PT arising from a single high-transmission channel. The best fit reveals $\tau = 0.99942 \pm 0.00006$ and $\Delta'/h = 25.2 \pm 0.2$ GHz. The manifestation of ABS with a very large transmission in single-tone spectroscopy in Fig. 4(b) is a sharp peak at $\varphi = \pi$ [24]. This feature is well described within the presented model with $\Phi_{\text{zpf}} = (0.0247 \pm 0.0002)\Phi_0$ as the only fitting parameter, and we extract the maximum coupling $g_c/2\pi = 1.95 \pm 0.02$ GHz at $\varphi = \pi$. We note that the extracted coupling indicates that the system is beyond the applicability of the perturbative approach. This explains a noticeable fit deviation in Fig. 4(b). At this level of consideration, the extracted coupling should be perceived as an approximate value.

B. Spectroscopy of single-quasiparticle transitions

SQPTs associated with spin-orbit-split ABSs were routinely observed for devices 2 and 3 with longer weak links.

Figures 5(a)–5(d) provide the spectroscopy data obtained for device 3 at $V_g = 1.498$ V and for device 2 at $V_g = 2.44$ V around the degeneracy points $\varphi = 0$ and $\varphi = \pi$, respectively. Figures 5(a) and 5(b) illustrate two-tone spectroscopy data that reveal bundles of four lines, which we assign to spin-conserving SQPTs [see Fig. 1(e)].

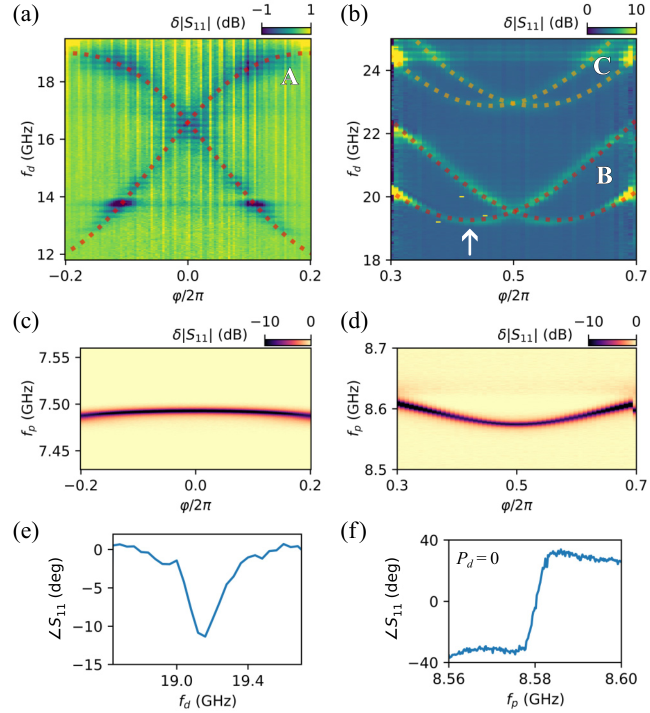

FIG. 5. (a)–(d) Spectroscopy data obtained for (a),(c) device 3 at $V_g = 1.498$ V and (b),(d) device 2 at $V_g = 2.44$ V. (a),(b) In two-tone spectra, bundles of SQPTs are observed, with crossings at the degeneracy points. SQPT frequency fits are denoted by the dotted lines and labeled as A, B, and C. The fit parameters are listed in Table II. (c),(d) The corresponding single-tone spectra. (e) Phase of the reflected signal as a function of the drive frequency at a minimum of the lower SQPT [see the white arrow in panel (b)]. (f) The corresponding resonator response when the system is not excited.

The spectroscopic lines in Fig. 5(a) can be fitted with the transitions between the two lowest Andreev doublets ($1\uparrow \Rightarrow 2\uparrow$ and $1\downarrow \Rightarrow 2\downarrow$). Parameters which provide the best fit were obtained by the least-squares method applied to transitions between the ABSs given by Eq. (1); see Appendix C for details. These parameters are listed in Table II, column A. The fit is shown by the red dotted line.

In Fig. 5(b), two bundles of lines are observed. Each of those take place at relatively large frequencies above 19 GHz and have an upward curved shape, implying that

TABLE II. A table of parameters for the SQPT fits in Figs. 5(a) and 5(b). The Δ_{Al}/h value is fixed at 52 GHz. See main text for meaning of column headings.

	A	B	C
Λ_1	5.7 ± 0.3	2.44 ± 0.07	2.8 ± 0.1
Λ_2	1.5 ± 0.3	3.06 ± 0.09	3.2 ± 0.1
τ	0.35 ± 0.04	0.243 ± 0.009	0.265 ± 0.006
x_0	0.489 ± 0.005	0.2615 ± 0.0001	-0.000837

the transitions occur between the upper doublets ($2\uparrow \Rightarrow 3\uparrow$ and $2\downarrow \Rightarrow 3\downarrow$). The parameters provided by the least-squares method are listed in Table II, where B corresponds to the red dotted line, and C to the orange one in Fig. 5(b), respectively.

The coupling between the resonator and a spinful ABS can be estimated from the line shape of an SQPT. Figure 5(e) shows the phase of the reflected signal as a function of the drive frequency at a minimum of the lower SQPT in Fig. 5(b) (marked by an arrow). The phase shift induced by this transition is $\delta(\angle S_{11}) \approx 10^\circ$. Based on the corresponding resonance line shape of a nonexcited system [Fig. 5(f)], the phase shift can be converted to the resonator frequency shift $\delta f_r^{\text{SQPT}} \approx 770$ kHz. It can be described by second-order perturbation theory [21] as

$$\delta f_r^{\text{SQPT}} \approx \left(\frac{g_c}{2\pi}\right)^2 \frac{2f_{\text{SQPT}}}{f_{\text{SQPT}}^2 - f_r^2},$$

from which we extract the spin-photon coupling $g_c/2\pi \approx 77$ MHz. This value is comparable to the recently reported strong coupling between a high-impedance resonator and a singlet-triplet spin qubit [35] and to the previously reported spin-photon coupling in InAs nanowire weak links [21].

We note that a more rigorous assessment of the coupling requires measurements of parity-switching dynamics in the system, which is a subject for further investigation. If the nonequilibrium quasiparticle poisoning is weak, the system resides in an odd-parity state [15,24,36,37] for only a small fraction of time, during which an SQPT can be excited. This can reduce the signal obtained in the spectroscopy of spin-orbit-split ABSs.

In our experiment, we repeatedly observed that only spin-conserving SQPTs are clearly visible in the spectra. This is in agreement with the general selection rules: in the presence of transverse symmetry in the nanowire, spin-flipping transitions should be suppressed. However, previous studies showed that spin-flipping transitions can still be excited at elevated drive powers in a realistic nonideal device [19,21]. For example, the gate drive can violate transverse symmetry and unlock spin-flipping transitions [24,38,39]. Although we used the gate drive in our setup, we did not observe spin-flipping SQPTs. This is most likely because we had to operate at sufficiently low drive powers, so that the thin-film resonator is not driven into a nonlinear regime.

IV. CONCLUSION

In conclusion, we have demonstrated a robust approach for achieving a large coupling strength between a high-impedance lumped-element resonator and ABSs residing in an InAs nanowire weak link. Moreover, we have shown that our geometry is suitable for the investigation of spin-orbit-split ABSs and the associated Andreev spin qubits. The presented approach can be further extended to facilitate a strong qubit-qubit coupling in a device comprising multiple Andreev qubits.

ACKNOWLEDGMENTS

This work was financially supported by the European Union's H2020 Research and Innovation Program, Grants No. 804988 (SiMS) and No. 828948 (AndQC), and by the Army Research Office (ARO), Grant No. W911NF2210053. The Center for Quantum Devices is supported by the Danish National Research Foundation, Grant No. DNRF101, by the Novo Nordisk Foundation, project SolidQ, and by the Carlsberg Foundation. The devices were fabricated in the Myfab cleanroom at Chalmers, and technical support from the Nanofabrication Laboratory is gratefully acknowledged. We also thank P. Makk, S. Csonka, G. Fülöp, and V. Fatemi for fruitful discussions.

DATA AVAILABILITY

The data that support the findings of this article are openly available [40].

APPENDIX A: NbTiN THIN-FILM HIGH KINETIC INDUCTANCE AND THE RESONATOR IMPEDANCE

The dc transport characterization of a test resonator structure (a replica of device 1) provides NbTiN thin-film normal-state sheet resistance $R_{N,\square} = 1.46$ kΩ and critical temperature $T_c = 6$ K. With these parameters, we can estimate the sheet kinetic inductance as $L_{k,\square}^{\text{dc}} \approx \hbar R_N/\pi\Delta$ [41], where $\Delta \approx 1.76 k_B T_c$ is the superconducting gap linked to T_c by a standard BCS prediction [42]. This yields $L_{k,\square}^{\text{dc}} \approx 320$ pH.

In addition, for each of the devices, we performed microwave domain simulations for the actual geometries used in the experiment. To simulate a bare resonator, we replaced the weak links with a short break in the film, but all the aluminum structures were included because they contribute to the total stray capacitance of the resonator. We extracted $L_{k,\square}$ from the best fits of the simulated resonator microwave response to the experimental data at low V_g, when the nanowires are fully depleted. The results are listed in Table I in the main text. Since all resonators were picked up from the same batch with the same NbTiN thickness, we attribute the variation in $L_{k,\square}$ to the aging of the sample and slightly different fabrication parameters used during nanowire processing (e.g., it was observed that the resulting $L_{k,\square}$ depends on the baking temperature of the resist).

The total inductance L_r (for one arm of the differential pair) is derived from the geometry and $L_{k,\square}$ is obtained as described above. The bare resonator frequency f_r is obtained experimentally. The differential impedance is defined as $Z_{r,\text{diff}} = 2\sqrt{L_r/C_r} = 4\pi f_r L_r$.

We note that we routinely observed the resonator's even mode, which is insensitive to the weak link's state and positioned at several hundred megahertz below the odd mode, yielding a flat line at around 8.1 GHz in Fig. 3. We confirmed the even-mode frequency by microwave domain simulations. Its frequency is determined by $2\pi f_r^{\text{even}} = 1/\sqrt{(L_r + 2L_{\text{gr}})C_r}$, where $L_{\text{gr}} \approx 10$ nH is the inductance of the grounding strip, which connects the ground plane and the middle part of the resonator [see Figs. 1(a) and 1(d)].

APPENDIX B: MEASUREMENT SETUP

The measurement scheme is similar to the one described in Ref. [43] and depicted in Fig. 6(a). The microwave readout tone passes through an attenuated line and a double circulator located at the mixing chamber stage, and is then routed through a 180° hybrid to differentially drive two on-chip 50-Ω feedlines capacitively coupled to the resonator. The readout tone is reflected off the resonator's odd mode and routed through a series of cryogenic and room-temperature amplifiers. The complex reflection parameter (S_{11}) is measured by a vector network analyzer. A separate microwave tone passes through the gate line to drive the ABS transitions, where a bias tee is used to combine the dc gate voltage and the drive tone.

Figures 6(b) and 6(c) represent the characteristic S_{11} response of one of the devices when the ABSs are far detuned (at zero applied flux). The resonance is fitted by the diameter-correction method [44], which yields the internal quality factor $Q_i \approx 3800$ and the coupling quality factor $Q_c \approx 1000$ when the ABSs are far detuned. We would like to emphasize that, in our setup, the large coupling magnitude results in a significant magnetic flux dependence of the internal quality factor when the Andreev level energy approaches the bare resonator frequency. At $\varphi = \pi$ the nanowire introduces maximum losses to the system, and Q_i usually drops to around 1000.

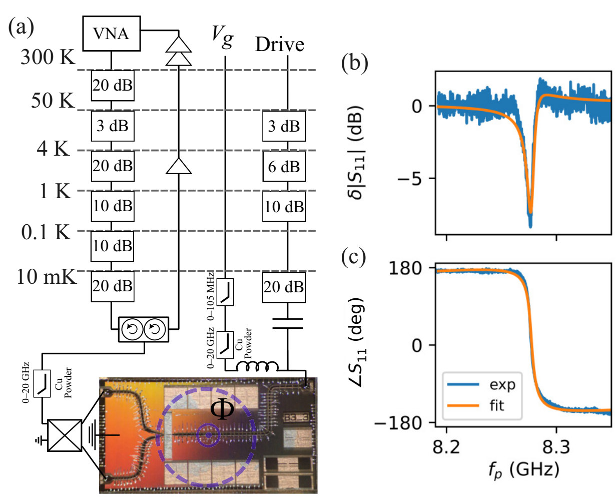

FIG. 6. (a) Experimental setup. (b),(c) Reflected signal amplitude (phase) versus probe tone frequency for one of the devices at zero external flux (the ABSs are far detuned). The blue line shows the experimental data. The orange line represents the fit, revealing that $Q_i \approx 3800$ and $Q_c \approx 1000$.

APPENDIX C: DETAILS OF THE FITTING ROUTINE

1. SQPTs

The SQPT frequency can be found from Eq. (1) in the main text as the difference between the energies of the two neighboring states. In our fitting routine, we first performed manual parameter selection to obtain a reasonable fit. Then, these parameters were used as an initial guess for the least-squares method. We found that the set of parameters is not always unique, which can produce large uncertainties. Furthermore, we frequently observed significant correlations between the parameters, such as the correlation between x_0 and Δ_{Al}, which could reach almost 100%. This is likely because both parameters are responsible for the overall energy scale. In order to mitigate these concerns, we fixed the gap parameter $\Delta_{\text{Al}}/h = 52$ GHz for all the fits depicted in Fig. 5. This appeared to be a satisfactory initial parameter guess for each fit.

2. PTs

The dispersion relation in Eq. (1) can be simplified to describe PTs in a finite-length weak link. For a PT, we detect the average of a spin-split Andreev doublet and we can neglect spin-orbit coupling assuming that $\Lambda_1 = \Lambda_2 = \Lambda$. Expansion of Eq. (1) around $\varphi = \pi$ up to second order in ϵ recovers the short-junction expression

$$E_A(\varphi) \approx \Delta' \sqrt{1 - \tau \sin^2(\varphi/2)}, \tag{C1}$$

with

$$\Delta' = \frac{\Delta_{\text{Al}}}{\sqrt{(1+\Lambda)^2 + (x_0 \Lambda \sqrt{1-\tau}\,)^2}}. \tag{C2}$$

To fit the resonator frequency shift in single-tone spectra, we use the perturbative model developed in Ref. [24]. This model relies on expansion of the Hamiltonian up to second order in Φ_{zpf}/Φ_0, which is still applicable to our strongly coupled system. The resonator shift is determined by the ABSs in the ground state, which is described by

$$\delta f_r = -2\left(\frac{\pi \Phi_{\mathrm{zpf}}}{\Phi_0}\right)^2 \frac{\partial^2 f_A}{\partial \varphi} + \left(\frac{g_c(\varphi)}{2\pi}\right)^2 \left(\frac{2}{f_A} - \frac{1}{f_A - f_r} - \frac{1}{f_A + f_r}\right), \qquad \text{(C3)}$$

with the phase-dependent coupling rate

$$\frac{g_c(\varphi)}{2\pi} = \frac{\Phi_{\mathrm{zpf}}}{\Phi_0}\sqrt{(1-\tau)}\left(-\frac{\partial f_A}{\partial \varphi}\right)\tan(\varphi/2), \qquad \text{(C4)}$$

where the pair transition frequency is expressed through its energy as $f_A(\varphi) = 2E_A(\varphi)/h$.

Here, we have introduced a single channel and neglected all the possible higher-energy states, including the continuum of states above the superconducting gap, which is known to contribute to the inductive response of a finite-length weak link [36,45]. We have also neglected the inductive energy of the shared inductance, which is generally true only when the supercurrent in the weak link is sufficiently small. However, this simple model demonstrated good correspondence between the extracted value of the coupling and the one directly observed in spectroscopy (e.g., in Fig. 3 in the main text), which justifies its validity.

In our fits, we used the least-squares method. When the single-tone spectra in Figs. 3(b) and 4(b) were fitted, the data set was multiplied by $f_A - f_r$ to eliminate the divergence in Eq. (C3).

APPENDIX D: RELATION BETWEEN THE PHASE ACROSS THE WEAK LINK AND THE APPLIED FLUX

In our devices, the loop inductance comprises the highly inductive NbTiN film with a total inductance of $2l \approx 10\,\mathrm{nH}$. When external flux is applied, part of the phase drops across the loop inductance, causing the self-screening effect [46],

$$\varphi = \frac{2\pi}{\Phi_0}(\Phi - 2lI_s), \qquad \text{(D1)}$$

where the supercurrent through the weak link is given by

$$I_s = \frac{-2e}{\hbar}\sum_p \frac{\partial E_A^p}{\partial \varphi}. \qquad \text{(D2)}$$

Here, the sum is taken over all ABSs with dispersions E_A^p. The full spectrum of ABSs residing in the weak link spans up to $2\Delta_{\mathrm{Al}}$ and, therefore, is usually not accessible in experiments.

However, it is possible to estimate the self-screening effect in the dispersive regime. Considering the circuit shown in Fig. 1(d) classically, we obtain the resonator frequency shift that arises from shunting the $2l$ part of the resonator inductance with the phase-dependent weak-link inductance $L_{\mathrm{wl}}(\varphi)$,

$$\frac{\delta f}{f_r} = -\frac{\delta L}{2(2L_r)}, \qquad \text{(D3)}$$

where $2L_r$ is the total resonator inductance and

$$\delta L = 2L_r - 2l + \frac{2lL_{\mathrm{wl}}}{2l + L_{\mathrm{wl}}} - 2L_r = -\frac{(2l)^2}{2l + L_{\mathrm{wl}}}. \qquad \text{(D4)}$$

Thus, the weak-link inductance can be directly retrieved from the single-tone spectra in the dispersive regime. The total supercurrent is related to the weak-link inductance as [47]

$$L_{\mathrm{wl}}(\varphi)^{-1} = \frac{2\pi}{\Phi_0}\frac{\partial I_s}{\partial \varphi}. \qquad \text{(D5)}$$

We analyze the self-screening effect, using the single-tone spectroscopy data obtained for device 3 at $V_g = 1.5034\,\mathrm{V}$ [see Fig. 7(a)]. In this regime, no avoided crossing is observed, but the resonator shift is reasonably large (about 150 MHz), which implies that one or a few ABSs with moderate transmission are present in the weak link, resulting in a relatively large supercurrent. The frequency shift fit is obtained by introducing one channel with

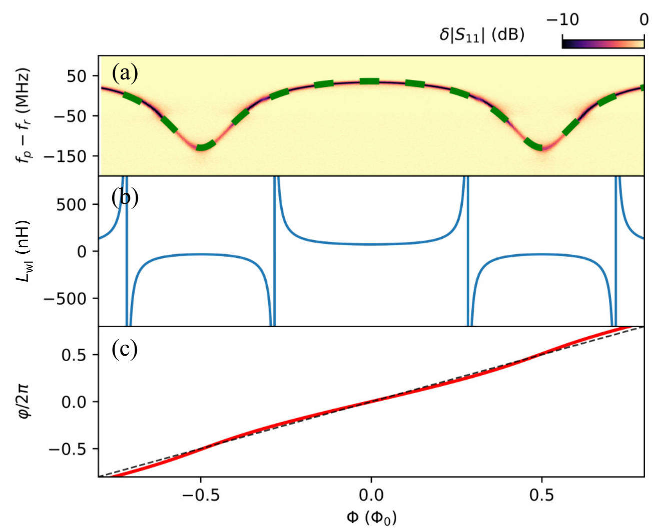

FIG. 7. (a) Single-tone spectrum measured in device 3 at $V_g = 1.5034\,\mathrm{V}$ offset to the bare resonator frequency $f_r = 7.4685$ GHz. The frequency shift fit as a function of applied flux is denoted by the green dashed line. (b) The corresponding weak-link inductance, derived from Eqs. (D3) and (D4). (c) The red line represents the phase across the weak link φ as a function of the applied flux Φ. For comparison, the black dashed line is plotted in the absence of self-screening ($2l = 0$).

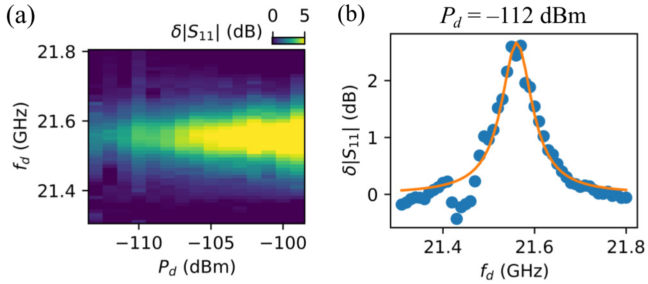

FIG. 8. (a) Power spectrum for device 3 at $V_g = 3.962$ V and $\varphi = 0$. (b) Line cut of panel (a) at low power $P_d = -112$ dBm with a Lorentzian fit.

$\Delta'/h = 17\,\mathrm{GHz}$, $\tau = 0.68$, and $\Phi_{\mathrm{zpf}} = 0.025\Phi_0$. Using Eqs. (D3) and (D4), we extract L_{wl} as a function of the applied flux [see Fig. 7(b)]. Further, under the assumption of negligible self-screening, $\varphi \approx 2\pi\Phi/\Phi_0$, we calculate the supercurrent by integrating Eq. (D5), and plug it into Eq. (D1) to estimate the self-screening. Figure 7(c) shows that $\varphi \approx 2\pi\Phi/\Phi_0$ was indeed a reasonable approximation, and self-screening can be neglected.

APPENDIX E: POWER SPECTRUM

Figure 8(a) represents the power spectrum, obtained for one of the PTs observed in device 2 at $\varphi = 0$. A low-power spectral line can be used to estimate the lower bound of the inhomogeneous dephasing time T_2^* in this device [48]. A line cut at $P_d = -112$ dBm is shown in Fig. 8(b). A Lorentzian fit to the spectral line fit reveals the full width at half maximum, $f_{\mathrm{FWHM}} \approx 82$ MHz. We estimate the lower bound of the inhomogeneous dephasing time as $T_2^* \gtrapprox 1/\pi f_{\mathrm{FWHM}} \approx 4$ ns, a smaller value compared to that previously reported in Ref. [15].

APPENDIX F: ADDITIONAL SPECTROSCOPY DATA

In this section, further data are provided for the devices.

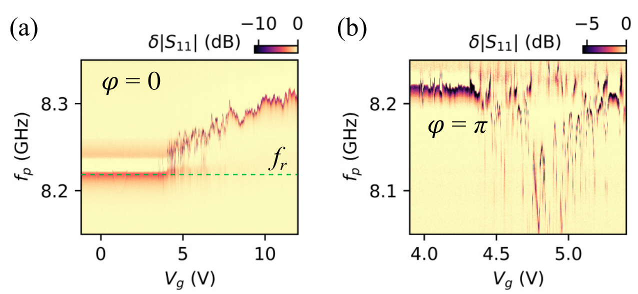

FIG. 9. Gate response measured in device 1 at (a) $\varphi = 0$ and (b) $\varphi = \pi$. The line at $f_r = 8.223$ GHz in panel (a) denotes the bare resonator frequency, when the nanowire is fully pinched off. The gate-independent background was subtracted.

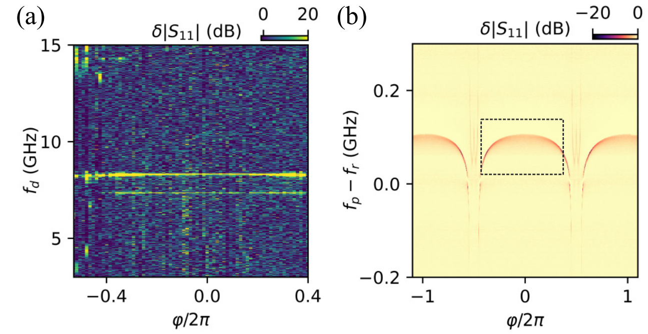

FIG. 10. Supplement to Fig. 4. (a) Two-tone spectrum measured in device 1 at $V_g = 14.5$ V. (b) The single-tone spectrum in a wide range of phase verifies the periodicity. The dashed rectangle denotes the range where panel (a) was measured.

1. Device 1

Figures 9(a) and 9(b) show the gate response of device 1 at $\varphi = 0$ and at $\varphi = \pi$, respectively. Figure 10 is a supplement to Fig. 4. The two-tone spectrum in Fig. 10(a) shows the lack of contributions from other higher-energy transitions, which justifies the use of the single-channel approximation in the fit in Fig. 4(b). The wide-range single-tone spectrum in Fig. 10(b) confirms the periodicity.

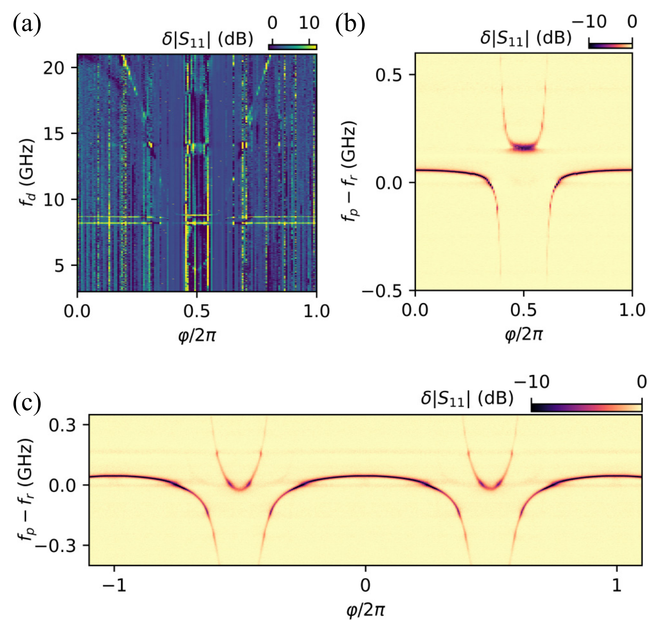

FIG. 11. Supplement to Fig. 3. (a) Two-tone spectrum measured in device 2 at $V_g = 3.39$ V. No higher-energy transitions are observed, which validates the single-channel model used in the fits. (b) The corresponding single-tone spectrum. (c) The single-tone spectrum at $V_g = 3.07\ V$ demonstrates periodicity.

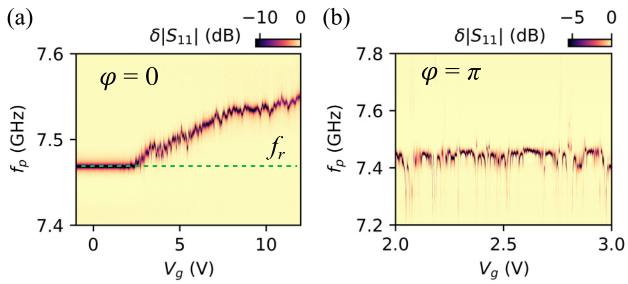

FIG. 12. Gate response measured in device 3 at (a) $\varphi = 0$ and (b) $\varphi = \pi$. The line at $f_r = 7.4685$ GHz in panel (a) denotes the bare resonator frequency, when the nanowire is fully pinched off. The gate-independent background was subtracted.

2. Device 2

Figure 11 is a supplement to Fig. 3. The two-tone spectrum in Fig. 11(a) demonstrates the absence of higher-energy transitions, which justifies the single-channel approximation used in the fit in Fig. 3(b). Figure 11(b) shows the corresponding single-tone spectrum. The wide range spectrum at $V_g = 3.07$ V in Fig. 11(c) confirms the periodicity.

3. Device 3

Figures 12(a) and 12(b) show the gate response of device 3 at $\varphi = 0$ and $\varphi = \pi$, respectively.

[1] A. Blais, A. L. Grimsmo, S. M. Girvin, and A. Wallraff, Circuit quantum electrodynamics, Rev. Mod. Phys. **93**, 025005 (2021).

[2] X. Mi, J. V. Cady, D. M. Zajac, P. W. Deelman, and J. R. Petta, Strong coupling of a single electron in silicon to a microwave photon, Science **355**, 156 (2016).

[3] J. Clarke and F. K. Wilhelm, Superconducting quantum bits, Nature **453**, 1031 (2008).

[4] A. Wallraff, D. I. Schuster, A. Blais, L. Frunzio, R.-S. Huang, J. Majer, S. Kumar, S. M. Girvin, and R. J. Schoelkopf, Strong coupling of a single photon to a superconducting qubit using circuit quantum electrodynamics, Nature **431**, 162 (2004).

[5] P. Forn-Díaz, L. Lamata, E. Rico, J. Kono, and E. Solano, Ultrastrong coupling regimes of light-matter interaction, Rev. Mod. Phys. **91**, 025005 (2019).

[6] A. Frisk Kockum, A. Miranowicz, S. De Liberato, S. Savasta, and F. Nori, Ultrastrong coupling between light and matter, Nat. Rev. Phys. **1**, 19 (2019).

[7] W. Qin, A. F. Kockum, C. S. Muñoz, A. Miranowicz, and F. Nori, Quantum amplification and simulation of strong and ultrastrong coupling of light and matter, Phys. Rep. **1078**, 1 (2024).

[8] T. Niemczyk, F. Deppe, H. Huebl, E. P. Menzel, F. Hocke, M. J. Schwarz, J. J. Garcia-Ripoll, D. Zueco, T. Hümmer, E. Solano, A. Marx, and R. Gross, Circuit quantum electrodynamics in the ultrastrong-coupling regime, Nat. Phys. **6**, 772 (2010).

[9] Y. Wang, C. Guo, G.-Q. Zhang, G. Wang, and C. Wu, Ultrafast quantum computation in ultrastrongly coupled circuit QED systems, Sci. Rep. **7**, 1 (2017).

[10] I. O. Kulik, Macroscopic quantization and the proximity effect in S-N-S junctions, Sov. J. Exp. Theor. Phys. **30**, 944 (1969).

[11] C. W. J. Beenakker and H. van Houten, Josephson current through a superconducting quantum point contact shorter than the coherence length, Phys. Rev. Lett. **66**, 3056 (1991).

[12] M. A. Despósito and A. Levy Yeyati, Controlled dephasing of Andreev states in superconducting quantum point contacts, Phys. Rev. B **64**, 140511(R) (2001).

[13] A. Zazunov, V. S. Shumeiko, E. N. Bratus', J. Lantz, and G. Wendin, Andreev level qubit, Phys. Rev. Lett. **90**, 087003 (2003).

[14] C. Janvier, L. Tosi, L. Bretheau, Ç. Ö. Girit, M. Stern, P. Bertet, P. Joyez, D. Vion, D. Esteve, M. F. Goffman, H. Pothier, and C. Urbina, Coherent manipulation of Andreev states in superconducting atomic contacts, Science **349**, 1199 (2015).

[15] M. Hays, G. de Lange, K. Serniak, D. J. van Woerkom, D. Bouman, P. Krogstrup, J. Nygård, A. Geresdi, and M. H. Devoret, Direct microwave measurement of Andreev-bound-state dynamics in a semiconductor-nanowire Josephson junction, Phys. Rev. Lett. **121**, 047001 (2018).

[16] P. Zellekens, R. S. Deacon, P. Perla, D. Grützmacher, M. I. Lepsa, T. Schäpers, and K. Ishibashi, Microwave spectroscopy of Andreev states in InAs nanowire-based hybrid junctions using a flip-chip layout, Commun. Phys. **5**, 1 (2022).

[17] N. M. Chtchelkatchev and Yu. V. Nazarov, Andreev quantum dots for spin manipulation, Phys. Rev. Lett. **90**, 226806 (2003).

[18] C. Padurariu and Yu. V. Nazarov, Theoretical proposal for superconducting spin qubits, Phys. Rev. B **81**, 144519 (2010).

[19] L. Tosi, C. Metzger, M. F. Goffman, C. Urbina, H. Pothier, S. Park, A. L. Yeyati, J. Nygård, and P. Krogstrup, Spin-orbit splitting of Andreev states revealed by microwave spectroscopy, Phys. Rev. X **9**, 011010 (2019).

[20] M. Hays, V. Fatemi, D. Bouman, J. Cerrillo, S. Diamond, K. Serniak, T. Connolly, P. Krogstrup, J. Nygård, A. L. Yeyati, A. Geresdi, and M. H. Devoret, Coherent manipulation of an Andreev spin qubit, Science **373**, 430 (2021).

[21] M. Hays, V. Fatemi, K. Serniak, D. Bouman, S. Diamond, G. de Lange, P. Krogstrup, J. Nygård, A. Geresdi, and M. H. Devoret, Continuous monitoring of a trapped superconducting spin, Nat. Phys. **16**, 1103 (2020).

[22] A. Bargerbos, M. Pita-Vidal, R. Žitko, L. J. Splitthoff, L. Grünhaupt, J. J. Wesdorp, Y. Liu, L. P. Kouwenhoven, R. Aguado, C. K. Andersen, A. Kou, and B. van Heck, Spectroscopy of spin-split Andreev levels in a quantum dot with superconducting leads, Phys. Rev. Lett. **131**, 097001 (2023).

[23] M. Pita-Vidal, A. Bargerbos, R. Žitko, L. J. Splitthoff, L. Grünhaupt, J. J. Wesdorp, Y. Liu, L. P. Kouwenhoven, R. Aguado, B. van Heck, A. Kou, and C. K. Andersen, Direct

manipulation of a superconducting spin qubit strongly coupled to a transmon qubit, Nat. Phys. **19**, 1110 (2023).
[24] C. Metzger, S. Park, L. Tosi, C. Janvier, A. A. Reynoso, M. F. Goffman, C. Urbina, A. Levy Yeyati, and H. Pothier, Circuit-QED with phase-biased Josephson weak links, Phys. Rev. Res. **3**, 013036 (2021).
[25] F. J. Matute-Cañadas, C. Metzger, S. Park, L. Tosi, P. Krogstrup, J. Nygård, M. F. Goffman, C. Urbina, H. Pothier, and A. L. Yeyati, Signatures of interactions in the Andreev spectrum of nanowire Josephson junctions, Phys. Rev. Lett. **128**, 197702 (2022).
[26] J. J. Wesdorp, F. J. Matute-Cañadas, A. Vaartjes, L. Grünhaupt, T. Laeven, S. Roelofs, L. J. Splitthoff, M. Pita-Vidal, A. Bargerbos, D. J. van Woerkom, P. Krogstrup, L. P. Kouwenhoven, C. K. Andersen, A. L. Yeyati, B. van Heck, and G. de Lange, Microwave spectroscopy of interacting Andreev spins, Phys. Rev. B **109**, 045302 (2024).
[27] P. Krogstrup, N. L. B. Ziino, W. Chang, S. M. Albrecht, M. H. Madsen, E. Johnson, J. Nygård, C. M. Marcus, and T. S. Jespersen, Epitaxy of semiconductor–superconductor nanowires, Nat. Mater. **14**, 400 (2015).
[28] M. Pita-Vidal, J. J. Wesdorp, and C. K. Andersen, Blueprint for all-to-all-connected superconducting spin qubits, PRX Quantum **6**, 010308 (2025).
[29] H. Lu, I. A. Day, A. R. Akhmerov, B. van Heck, and V. Fatemi, Kramers-protected hardware-efficient error correction with Andreev spin qubits, ArXiv:2412.16116 [quant-ph].
[30] S. Abay, D. Persson, H. Nilsson, F. Wu, H. Q. Xu, M. Fogelström, V. Shumeiko, and P. Delsing, Charge transport in InAs nanowire Josephson junctions, Phys. Rev. B **89**, 214508 (2014).
[31] M. H. Devoret, S. Girvin, and R. Schoelkopf, Circuit-QED: How strong can the coupling between a Josephson junction atom and a transmission line resonator be? Ann. Phys. **519**, 767 (2007).
[32] A. Stockklauser, P. Scarlino, J. V. Koski, S. Gasparinetti, C. K. Andersen, C. Reichl, W. Wegscheider, T. Ihn, K. Ensslin, and A. Wallraff, Strong coupling cavity QED with gate-defined double quantum dots enabled by a high impedance resonator, Phys. Rev. X **7**, 011030 (2017).
[33] J. E. Sestoft, M. Marnauza, D. Olsteins, T. Kanne, R. D. Schlosser, I.-J. Chen, K. Grove-rasmussen, and J. Nygård, Shadowed versus etched superconductor–semiconductor junctions in Al/InAs nanowires, Nano Lett. **24**, 8394 (2024).
[34] S. Park and A. L. Yeyati, Andreev spin qubits in multichannel Rashba nanowires, Phys. Rev. B **96**, 125416 (2017).
[35] J. H. Ungerer, A. Pally, A. Kononov, S. Lehmann, J. Ridderbos, P. P. Potts, C. Thelander, K. A. Dick, V. F. Maisi, P. Scarlino, A. Baumgartner, and C. Schönenberger, Strong coupling between a microwave photon and a singlet-triplet qubit, Nat. Commun. **15**, 1 (2024).
[36] V. Fatemi, P. D. Kurilovich, M. Hays, D. Bouman, T. Connolly, S. Diamond, N. E. Frattini, V. D. Kurilovich, P. Krogstrup, J. Nygård, A. Geresdi, L. I. Glazman, and M. H. Devoret, Microwave susceptibility observation of interacting many-body Andreev states, Phys. Rev. Lett. **129**, 227701 (2022).
[37] M. R. Sahu, F. J. Matute-Cañadas, M. Benito, P. Krogstrup, J. Nygård, M. F. Goffman, C. Urbina, A. L. Yeyati, and H. Pothier, Ground-state phase diagram and parity-flipping microwave transitions in a gate-tunable Josephson junction, Phys. Rev. B **109**, 134506 (2024).
[38] C. Metzger, Spin & charge effects in Andreev bound states, Ph.D. thesis, Service de physique de l'état condensé, France, Quantronics Group, France, Saclay, 2022.
[39] H. Lu, D. F. Bofill, Z. Sun, T. Kanne, J. Nygård, M. Kjaergaard, and V. Fatemi, Andreev spin relaxation time in a shadow-evaporated InAs weak link, Phys. Rev. Appl. **24**, 024046 (2025).
[40] O. Shvetsov, A. Khola, V. Buccheri, I. Cools, N. Trnjanin, T. Kanne, J. Nygård, and A. Geresdi, Dataset for "Approaching the ultrastrong coupling regime between an Andreev level and a microwave resonator", https://zenodo.org/records/17117780 (2025).
[41] A. J. Annunziata, D. F. Santavicca, L. Frunzio, G. Catelani, M. J. Rooks, A. Frydman, and D. E. Prober, Tunable superconducting nanoinductors, Nanotechnology **21**, 445202 (2010).
[42] J. Bardeen, L. N. Cooper, and J. R. Schrieffer, Theory of superconductivity, Phys. Rev. **108**, 1175 (1957).
[43] I. P. C. Cools, R. M. López-Báez, V. Buccheri, O. Shvetsov, N. Trnjanin, E. Hogedal, and S. P. Dash, Losses in magnetic field resilient coplanar stripline resonators, J. Phys. D: Appl. Phys. **58**, 255102 (2025).
[44] S. Probst, F. B. Song, P. A. Bushev, A. V. Ustinov, and M. Weides, Efficient and robust analysis of complex scattering data under noise in microwave resonators, Review of Scientific Instruments **86**, 024706 (2015).
[45] P. D. Kurilovich, V. D. Kurilovich, V. Fatemi, M. H. Devoret, and L. I. Glazman, Microwave response of an Andreev bound state, Phys. Rev. B **104**, 174517 (2021).
[46] P. Jung, S. Butz, S. V. Shitov, and A. V. Ustinov, Low-loss tunable metamaterials using superconducting circuits with Josephson junctions, Appl. Phys. Lett. **102**, 062601 (2013).
[47] A. Paila, D. Gunnarsson, J. Sarkar, M. A. Sillanpää, and P. J. Hakonen, Current-phase relation and Josephson inductance in a superconducting Cooper-pair transistor, Phys. Rev. B **80**, 144520 (2009).
[48] K. D. Petersson, J. R. Petta, H. Lu, and A. C. Gossard, Quantum coherence in a one-electron semiconductor charge qubit, Phys. Rev. Lett. **105**, 246804 (2010).